Non-Hermitian Dirac Cones

Haoran Xue,[1] Qiang Wang,[1] Baile Zhang,[1,2,*] and Y. D. Chong[1,2,†]
[1]Division of Physics and Applied Physics, School of Physical and Mathematical Sciences, Nanyang Technological University, Singapore 637371, Singapore
[2]Centre for Disruptive Photonic Technologies, Nanyang Technological University, Singapore 637371, Singapore

(Received 23 December 2019; accepted 21 May 2020; published 12 June 2020)

Non-Hermitian systems containing gain or loss commonly host exceptional point degeneracies, not the diabolic points that, in Hermitian systems, play a key role in topological transitions and related phenomena. Non-Hermitian Hamiltonians with parity-time symmetry can have real spectra but generally nonorthogonal eigenstates, impeding the emergence of diabolic points. We introduce a pair of symmetries that induce not only real eigenvalues but also pairwise eigenstate orthogonality. This allows non-Hermitian systems to host Dirac points and other diabolic points. We construct non-Hermitian models exhibiting three exemplary phenomena previously limited to the Hermitian regime: Haldane-type topological phase transition, Landau levels without magnetic fields, and Weyl points. This establishes a new connection between non-Hermitian physics and the rich phenomenology of diabolic points.

DOI: 10.1103/PhysRevLett.124.236403

Introduction.—If a Hamiltonian is Hermitian, its eigenstates form an orthogonal basis, even at eigenvalue degeneracies or "diabolic points." The presence of diabolic points has important implications [1–3] as their dynamics is described by elementary equations like the two-dimensional (2D) Dirac equation [4–6], which have nontrivial topological features. For instance, Dirac points in 2D band structures play a key role in transitions between topologically distinct insulator phases [7,8]. Recently, there has been much interest in degeneracies of non-Hermitian systems (i.e., systems with gain and/or loss) [9,10]. Non-Hermitian Hamiltonians typically have nonorthogonal eigenvectors and degeneracies that are exceptional points (EPs), where eigenvectors—not just eigenvalues—are degenerate [11]. This includes the special class of parity-time (PT) symmetric systems [12,13]. EPs give rise to many striking physical effects with applications ranging from waveguide mode conversion to optical sensing [12–21]. Despite the rich phenomenology of diabolic points in Hermitian systems, little attention has been paid to realizing them in the non-Hermitian regime, or the resulting implications. Previous works have shown only that diabolic points of Hermitian systems usually do not survive into the non-Hermitian regime [22–30]. Instead, they split into EPs [23] or evolve into "exceptional rings" [22,26].

This Letter proposes a mechanism for non-Hermitian systems to support symmetry-stabilized diabolic points, allowing them to access the phenomenology of Dirac points, Weyl points, and other topologically nontrivial band degeneracies [2]. Extending the earlier insight that non-Hermitian symmetries (e.g., PT symmetry) can sustain real eigenvalues [12], we formulate a set of non-Hermitian symmetries that provide not just real eigenvalues but also orthogonal eigenstates. We construct a family of non-Hermitian lattice models that satisfy these symmetries, and hence show how to use gain and loss to realize three exemplary phenomena normally restricted to the Hermitian regime. The first is a phase transition between topologically distinct 2D insulator phases, similar to the Haldane model [7] (a foundational model for the theory of topological band insulators [8]), except that the transition is driven by a gain or loss degree of freedom rather than a Hermitian degree of freedom like a lattice inversion-breaking parameter. The second is the formation of Landau levels by synthetic magnetic fields. It has previously been shown that Landau levels can be induced via "strain engineering"—i.e., applying special distortions to a lattice hosting Dirac points [31–33]. We show that the phenomenon can be achieved via gain and loss, without Hermitian lattice distortions. Finally, we demonstrate for the first time a non-Hermitian 3D model exhibiting Weyl points [2,34], with real bulk energies and Fermi arc surface states with complex energies.

Our approach differs from the recent spate of efforts [19,35–42] aimed at extending concepts of band geometry and topology to the non-Hermitian regime by formulating new topological invariants, topological classifications, bulk-boundary correspondences, etc. The non-Hermitian models we present acquire their interesting features not from novel topological principles, but from Dirac and Weyl points that act similarly (though not identically) to those in Hermitian systems. This establishes a new way to connect non-Hermitian physics with the physics of topological band structures, and may be useful for designing devices such as lasers that use gain or loss to achieve topological transitions, Landau levels, etc.

Non-Hermitian symmetries.—We first define the following 4×4 matrices:

$$\Sigma_\mu = \begin{bmatrix} 0 & \sigma_\mu \\ \sigma_\mu & 0 \end{bmatrix}, \qquad \mu = 0, 1, 2, 3. \tag{1}$$

Here, σ_0 denotes the 2×2 identity matrix and σ_j denotes the Pauli matrices for $j = 1, 2, 3$.

Let H be a 4×4 matrix, which needs not to be Hermitian, which satisfies (i) the pseudo-Hermiticity condition

$$\Sigma_0 H \Sigma_0 = H^\dagger, \tag{2}$$

and (ii) the anti-PT symmetry condition

$$\{H, \Sigma_3 \Sigma_1 T\} = 0, \tag{3}$$

where T is the complex conjugation operator.

Equation (2) implies that the eigenvalues of H are real or form complex conjugate pairs [43]. Equation (3) implies that the eigenvectors form orthogonal pairs: if $|\psi_+\rangle$ is an eigenvector of H with eigenvalue E_+, then $|\psi_-\rangle = \Sigma_1 \Sigma_3 T |\psi_+\rangle$ is an eigenvector with eigenvalue $-E_+^*$, and $|\psi_+\rangle$ and $|\psi_-\rangle$ can be shown to be orthogonal [44]:

$$\langle \psi_+ | \psi_- \rangle = \sum_{n=1}^{4} (\psi_+^n)^* \psi_-^n = 0. \tag{4}$$

The proof of this uses the specific form of $\Sigma_1 \Sigma_3$, and the fact that $\langle \varphi | \sigma_2 T | \varphi \rangle = 0$ for any two-component $|\varphi\rangle$.

With both symmetries present, the eigenvalues either form the set $\{z, z^*, -z, -z^*\}$ for nonreal z (the symmetry-broken case), or two real pairs $\{E_1, -E_1\}$ and $\{E_2, -E_2\}$ where the eigenvectors in each pair are orthogonal but eigenvectors in different pairs are generally nonorthogonal (the symmetry-unbroken case). The latter regime supports the possibility of diabolic points.

A matrix satisfying Eqs. (2) and (3) has the form

$$H = \begin{bmatrix} \mathcal{W} & \mathcal{V}_+ \\ \mathcal{V}_- & \mathcal{W}^\dagger \end{bmatrix}, \tag{5}$$

$$\mathcal{W} = \begin{bmatrix} a & b \\ b^* & -a^* \end{bmatrix}, \qquad \mathcal{V}_\pm = \begin{bmatrix} \lambda_\pm & c_\pm \\ c_\pm^* & -\lambda_\pm \end{bmatrix}, \tag{6}$$

where a, b, $c_\pm \in \mathbb{C}$, and $\lambda_\pm \in \mathbb{R}$.

Lattice model.—Consider the honeycomb lattice shown in Fig. 1(a). The lattice sites have complex on-site mass terms; the real parts $\pm m$ are indicated by thick and thin outlines, and the imaginary parts $\pm\gamma$ (i.e., on-site gain or loss) are indicated by red and blue colors. Let the nearest-neighbor intersite couplings be $t_1 = 1$, and take Haldane-type next-nearest-neighbor couplings with magnitude t_2 and phase $-\pi/2$ [7]. For $\gamma \neq 0$, the lattice is non-Hermitian and each unit cell has four sites, with lattice vectors $a_1 = [1, 0]$ and $a_2 = [0, \sqrt{3}]$.

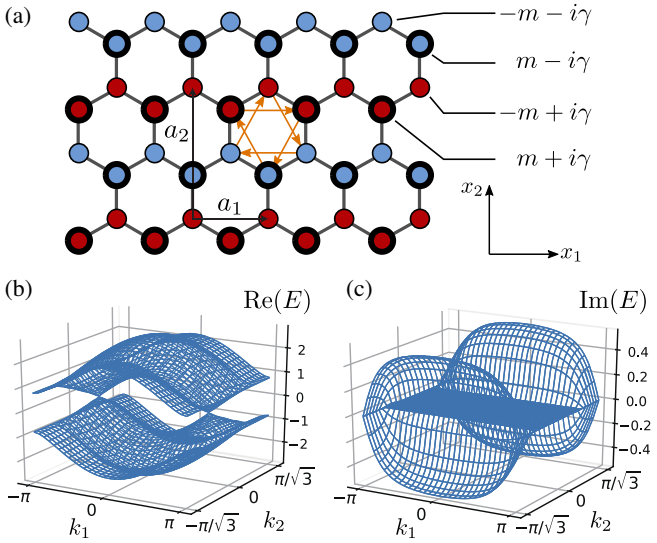

FIG. 1. (a) Schematic of the non-Hermitian lattice. Thick (thin) circle outlines indicate positive (negative) real parts of the on-site mass terms, $\pm m$, while red (blue) colors indicate positive (negative) imaginary parts, $\pm i\gamma$. The nearest-neighbor coupling is $t_1 = 1$. Orange arrows indicate the next-nearest-neighbor couplings of $\mp i t_2$ along (opposite to) the arrow; for clarity, only couplings in one hexagon are depicted. Black arrows show the elementary lattice vectors a_1 and a_2. (b)–(c) Complex band structure for $m = 0$ and $\gamma = 0.6$.

The k-space Hamiltonian satisfies Eqs. (5)–(6) with

$$\begin{aligned} a &= m + i\gamma + 2t_2 \sin k_1, \\ b &= 2 \cos(k_1/2) \exp[i k_2/(2\sqrt{3})], \\ \lambda_\pm &= -4t_2 \sin(k_1/2) \cos(\sqrt{3} k_2/2), \\ c_\pm &= \exp(-i k_2/\sqrt{3}). \end{aligned} \tag{7}$$

Thus, Eqs. (2) and (3) hold for all k. If the next-nearest-neighbor couplings are nonzero and have phases other than $\pm\pi/2$, $H(k)$ would not satisfy the symmetries.

The spectrum of $H(k)$ can be derived analytically for $m = t_2 = 0$ [44]. For $|\gamma| < 1$, all four eigenvalues are real for $|k_2| < \cos^{-1}(2\gamma^2 - 1)/\sqrt{3}$; in the symmetry-unbroken domain, $E = 0$ degeneracies occur at

$$K^\tau = \begin{pmatrix} -2\tau\theta \\ 0 \end{pmatrix}, \quad \text{where} \begin{cases} \tau & = \pm 1, \\ \cos 2\theta & = (-1 - \gamma^2)/2. \end{cases} \tag{8}$$

Figures 1(b)–1(c) show the band structure for $m = t_2 = 0$ and $\gamma = 0.6$, with the degeneracy points clearly visible.

There are two orthogonal eigenstates at each degeneracy point, so these are diabolic points, not EPs. Figures 1(b)–1(c) shows that the spectrum is linear near each degeneracy point,

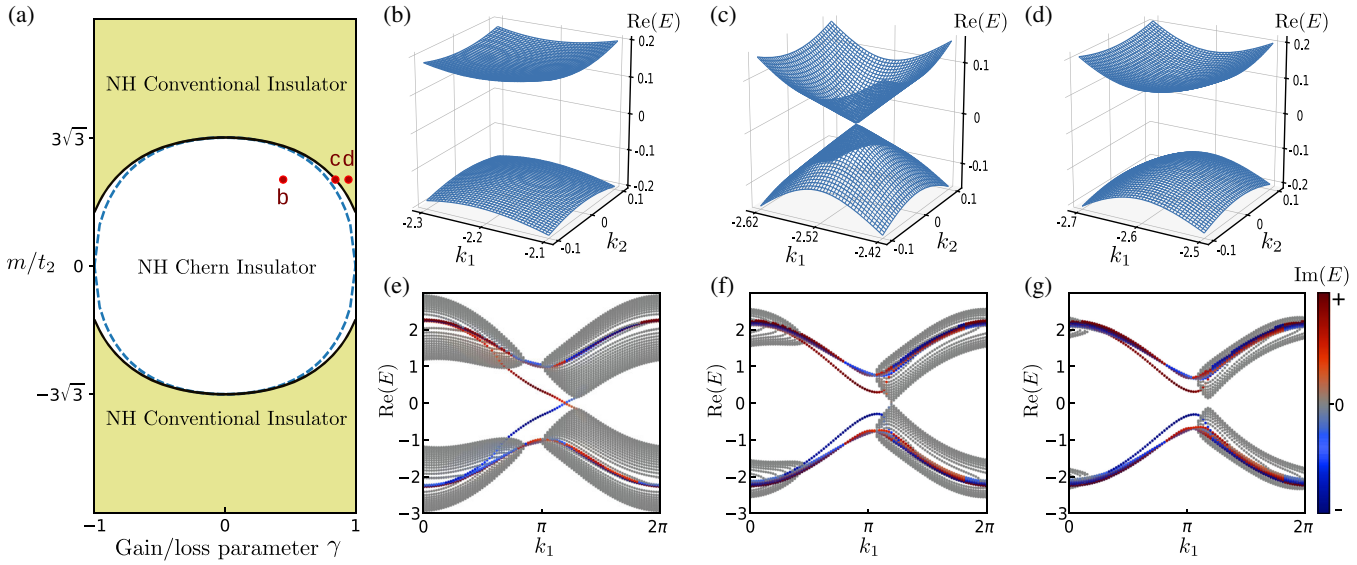

FIG. 2. (a) Phase diagram of the 2D non-Hermitian lattice, featuring a non-Hermitian Chern insulator phase (white) and a non-Hermitian conventional insulator phase (yellow). Black curves are phase boundaries computed by varying m and γ for fixed $t_2 = 0.1$ and searching numerically for band degeneracies. Blue dashes are analytical phase boundaries given by Eq. (12). Red dots indicate the points corresponding to the (b)–(d) subplots. (b)–(d) Bulk band diagrams near one of the K^τ points. The lattice parameters are $t_2 = 0.1$, $m = 0.35$, and $\gamma = 0.846 + \delta\gamma$ where $\delta\gamma = -0.4$ for (b), $\delta\gamma = 0$ for (c), and $\delta\gamma = 0.1$ for (d). All depicted eigenvalues have a zero imaginary part. (e)–(g) Band diagrams for a strip infinite in x_1 and 25 cells wide in x_2, using the parameters of (b)–(d). Colors represent the imaginary part of the energy eigenvalues.

indicating that they are Dirac points. To prove this, let $q = (q_1, q_2)$ be the displacement relative to K^τ, let $|\psi\rangle = [|\varphi_+\rangle, |\varphi_-\rangle]$ be an eigenstate with energy E, and let E, m, and t_2 be of order q. To first order, $|\varphi_\pm\rangle$ are found to be governed by [44]

$$v(\tau\eta_\gamma\sigma_1 q_1 - \sigma_2 q_2 + M\sigma_3)U_\pm|\varphi_\pm\rangle = EU_\pm|\varphi_\pm\rangle + \cdots. \quad (9)$$

Here $v = \sqrt{3}/2$ is the Dirac velocity, $\eta_\gamma = 2\sin\theta/\sqrt{3}$ is an anisotropy parameter that goes to 1 when $\gamma \to 0$, and

$$U_\pm = \exp\left[\pm\frac{i}{2}(\sin^{-1}\gamma)\sigma_1\right], \quad (10)$$

$$M = \frac{m - 6\tau t_2 \sin 2\theta}{2\cos\theta}. \quad (11)$$

This result only applies to the two bands involved in the degeneracy point. The other two do not satisfy $E \sim O(q)$, so Eq. (9) does not apply.

Non-Hermitian gapped phases.—For $t_2 \neq 0$, the model exhibits two types of gapped phases. If the term proportional to τt_2 in Eq. (11) dominates the term proportional to m, the Dirac cones have opposite mass, and if the reverse is true, the Dirac cones have the same mass. This is similar to the Chern insulator and conventional insulator phases of the Haldane model [7]. The phase transition is predicted to occur at

$$|m| = 3|t_2|\sqrt{(3+\gamma^2)(1-\gamma^2)}. \quad (12)$$

At the transition point, there is an unpaired Dirac cone at one of the K^τ points, similar to the transition described in the Haldane model [7].

The phase diagram is shown in Fig. 2(a). The predicted phase boundaries of Eq. (12) agree with those found by numerically searching for band degeneracies, with the discrepancies diminishing as t_2 is further reduced. The shape of the transition curve raises the interesting possibility of driving a phase transition entirely via gain and loss. As indicated by the points labeled b–d in Fig. 2(a), we can fix nonzero values of m and t_2 and increase γ from zero, and thereby change the system from a non-Hermitian Chern insulator (which reduces to a Hermitian Chern insulator for $\gamma = 0$) into a non-Hermitian conventional insulator [Figs. 2(b)–2(d)].

The two gapped bulk phases are accompanied by edge state behaviors similar to Hermitian Chern and conventional insulators, as seen in Figs. 2(e)–2(g). The non-Hermitian Chern insulator hosts edge states spanning the gap, arising from the fact that the non-Hermitian k-space Hamiltonian has effective 2D Dirac solutions to which the standard topological bulk-edge correspondence applies. The truncation of the real-space lattice breaks the symmetries Eqs. (2)–(3), so that the edge state energies acquire substantial imaginary parts; these values depend on the choice of boundary termination, and in the case of Figs. 2(e)–2(g)

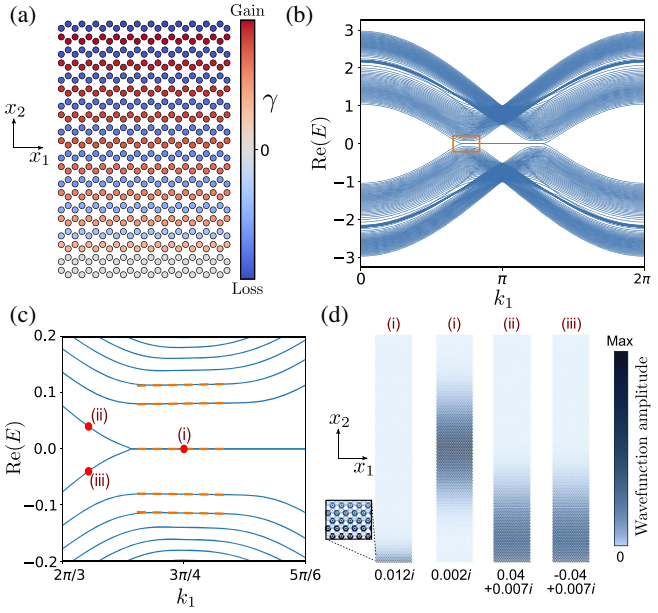

FIG. 3. (a) Schematic of a 2D strip with gain and loss distributed as $\theta = \theta_0 + \beta x_2$. The strip is infinite along x_1. (b) Real part of the band diagram for a strip 300 sites wide along x_2, with $\beta = 0.002$. (c) Close-up of the band diagram near one of the projected K^τ points, showing the formation of Landau levels. Horizontal dashes indicate the energies for the lowest few Landau levels derived from a continuum Dirac theory with a pseudomagnetic field. (d) Wave function amplitude distributions for the four eigenstates indicated by (i)–(iii) in (c). The numbers below indicate the energy eigenvalues.

range from around -0.9 to 0.9. For most of the bulk states, the energies are almost exactly real.

Non-Hermitian pseudomagnetic fields.—The non-Hermitian Dirac cones can experience pseudomagnetic fields similar to those found in Hermitian lattices [31–33], except that these pseudomagnetic fields can be induced by gain and loss engineering rather than strain engineering. For $m = t_2 = 0$, the Dirac cones are ungapped; since their k-space positions depend on γ [Eq. (8)], a spatial variation in γ acts as a gauge field. By analogy, in Hermitian graphenelike lattices a spatially uniform change in the coupling terms shifts the Dirac points in k space, so a nonuniform variation acts as a valley-specific gauge field that induces Landau levels [31–33].

Figure 3(a) shows a lattice that is infinite in x_1 and finite in x_2. Since the k-space displacement of the Dirac point is proportional to θ [Eq. (8)], we vary γ so that $\theta[\gamma(x_2)] = \theta_0 + \beta x_2$. A theoretical analysis [44] shows that the system hosts a zeroth Landau level (a flat band at $E = 0$), and bands similar to nonzero Landau levels. The computed band diagram is shown in Figs. 3(b)–3(c). The zeroth Landau level is clearly present, and the energies of the nonzero bands also match theoretical predictions. Figure 3(d) plots the wave function amplitude distributions for four eigenstates labelled (i)–(iii) in Fig. 3(c). The eigenstates at (i) are two

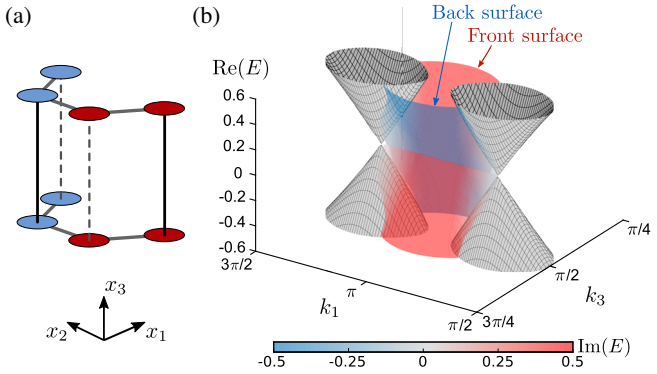

FIG. 4. (a) 3D non-Hermitian lattice hosting Weyl points. Solid (dashed) lines indicate positive (negative) couplings $\pm t_3$. (b) Surface dispersion for a slab with periodic boundary conditions along x_1 and x_3, and open boundaries along x_2. The lattice parameters are $t_1 = t_3 = 1$, $t_2 = m = 0$, and $\gamma = 0.6$.

fold degenerate, and consist of a bulk mode and an edge mode; those at (ii) and (iii) are edge modes connected to the zeroth Landau level. We emphasize that the flat bands are generated by spatial variations in gain and loss, without strain engineering [54,55] or a real magnetic field. We have performed full-wave simulations demonstrating that gain and loss controlled Laudau levels can be observed experimentally as narrow peaks in transmission spectra [44]. They may be useful for slow light applications [56], and for enhancing optical nonlinearity [57].

Non-Hermitian Weyl points.—The present framework for generating diabolic points in non-Hermitian systems is not limited to Dirac points in 2D lattices. We can formulate a non-Hermitian 3D lattice model exhibiting Weyl points, the simplest 3D diabolic points.

The lattice, shown in Fig. 4(a), is constructed by stacking copies of the previous 2D lattice with $m = t_2 = 0$. Along x_3, the positive (negative) interlayer couplings are indicated by solid (dashed) lines. The lattice Hamiltonian then satisfies Eqs. (5)–(6); for each k_3, the interlayer couplings act as m. For $\gamma = 0$, this is a Weyl semimetal [45]. Upon varying γ, the Weyl points shift in momentum space, raising the possibility of gain or loss induced chiral Landau levels [58]. Figure 4(b) shows the formation of complex-valued Fermi arcs, whose real parts connect the projections of the real-valued bulk Weyl cones.

Discussion.—We have shown that diabolic points can occur in non-Hermitian systems by using symmetry constraints to enforce eigenstate orthogonality. This allows for non-Hermitian systems that exhibit the rich phenomenology of diabolic points, as illustrated by the three striking examples presented above—topological transitions in two dimensions, Landau levels without magnetic fields, and Weyl points. These models are not the only ones that can achieve such outcomes; it would be desirable to find a general description of all such non-Hermitian models. It will also be interesting to study the properties of other

non-Hermitian diabolic points, such as quadratic band degeneracies [59], type-II Weyl points [60], higher order Weyl points [3,61], and nodal lines [62].

These theoretical ideas can be realized using a variety of experimental platforms. We have performed full-wave simulations of coupled acoustic resonator arrays [45–50] with appropriate gain and loss, and found that such structures can manifest the experimental signatures of gain and loss induced Landau levels or Weyl points, consistent with the above tight-binding models [44]. Laser-written optical waveguide arrays [63] are another promising platform; it has been shown that waveguide losses in these arrays can be individually customized (to realize non-Hermitian bulk topological transitions [64] or Weyl exceptional rings [26]), while T can be effectively broken by twisting the waveguides [60,65]. Electric circuits, which have been used to demonstrate various topological and non-Hermitian models [66–68], can also be used to implement the models. Finally, it would be exciting to pursue realizations using active nanophotonic platforms, such as resonator arrays [69–72] with actively tunable gain or loss. A longstanding obstacle to applying strain engineering ideas [31] to photonics is the impracticality of mechanically deforming photonic devices. The present scheme allows for using active gain or loss to, for example, strongly alter the photonic density of states on demand.

We are grateful to M. C. Rechtsman for helpful discussions. This work was supported by the Singapore MOE Academic Research Fund Tier 3 Grant No. MOE2016-T3-1-006, Tier 1 Grant No. RG187/18 and Tier 2 Grant No. MOE 2018-T2-1-022(S).

*blzhang@ntu.edu.sg
†yidong@ntu.edu.sg

[1] A. H. Castro Neto, F. Guinea, N. M. R. Peres, K. S. Novoselov, and A. K. Geim, Rev. Mod. Phys. **81**, 109 (2009).
[2] N. P. Armitage, E. J. Mele, and A. Vishwanath, Rev. Mod. Phys. **90**, 015001 (2018).
[3] B. Bradlyn, J. Cano, Z. Wang, M. Vergniory, C. Felser, R. J. Cava, and B. A. Bernevig, Science **353**, aaf5037 (2016).
[4] K. S. Novoselov, A. K. Geim, S. V. Morozov, D. Jiang, M. I. Katsnelson, I. V. Grigorieva, S. V. Dubonos, and A. A. Firsov, Nature (London) **438**, 197 (2005).
[5] S.-Y. Xu, I. Belopolski, N. Alidoust, M. Neupane, G. Bian, C. Zhang, R. Sankar, G. Chang, Z. Yuan, C.-C. Lee *et al.*, Science **349**, 613 (2015).
[6] L. Lu, Z. Wang, D. Ye, L. Ran, L. Fu, J. D. Joannopoulos, and M. Soljačić, Science **349**, 622 (2015).
[7] F. D. M. Haldane, Phys. Rev. Lett. **61**, 2015 (1988).
[8] A. Bansil, H. Lin, and T. Das, Rev. Mod. Phys. **88**, 021004 (2016).
[9] C. Bender, Rep. Prog. Phys. **70**, 947 (2007).
[10] N. Moiseyev, *Non-Hermitian Quantum Mechanics* (Cambridge University Press, Cambridge, 2011).
[11] T. Kato, *Perturbation Theory for Linear Operators* (Springer, New York, 1966).
[12] C. M. Bender and S. Boettcher, Phys. Rev. Lett. **80**, 5243 (1998).
[13] L. Feng, R. El-Ganainy, and L. Ge, Nat. Photonics **11**, 752 (2017).
[14] R. El-Ganainy, K. G. Makris, M. Khajavikhan, Z. H. Musslimani, S. Rotter, and D. N. Christodoulides, Nat. Phys. **14**, 11 (2018).
[15] M.-A. Miri and A. Alù, Science **363**, eaar7709 (2019).
[16] Z. Lin, H. Ramezani, T. Eichelkraut, T. Kottos, H. Cao, and D. N. Christodoulides, Phys. Rev. Lett. **106**, 213901 (2011).
[17] C. Dembowski, H.-D. Gräf, H. L. Harney, A. Heine, W. D. Heiss, H. Rehfeld, and A. Richter, Phys. Rev. Lett. **86**, 787 (2001).
[18] J. Wiersig, Phys. Rev. Lett. **112**, 203901 (2014).
[19] D. Leykam, K. Y. Bliokh, C. Huang, Y. D. Chong, and F. Nori, Phys. Rev. Lett. **118**, 040401 (2017).
[20] K. Kawabata, T. Bessho, and M. Sato, Phys. Rev. Lett. **123**, 066405 (2019).
[21] Z. Yang, A. Schnyder, J. Hu, and C.-K. Chiu, arXiv: 1912.02788.
[22] B. Zhen, C. W. Hsu, Y. Igarashi, L. Lu, I. Kaminer, A. Pick, S.-L. Chua, J. D. Joannopoulos, and M. Soljačić, Nature (London) **525**, 354 (2015).
[23] H. Zhou, C. Peng, Y. Yoon, C. W. Hsu, K. A. Nelson, L. Fu, J. D. Joannopoulos, M. Soljačić, and B. Zhen, Science **359**, 1009 (2018).
[24] Y. Xu, S.-T. Wang, and L.-M. Duan, Phys. Rev. Lett. **118**, 045701 (2017).
[25] A. Cerjan, M. Xiao, L. Yuan, and S. Fan, Phys. Rev. B **97**, 075128 (2018).
[26] A. Cerjan, S. Huang, M. Wang, K. P. Chen, Y. Chong, and M. C. Rechtsman, Nat. Photonics **13**, 623 (2019).
[27] J. C. Budich, J. Carlström, F. K. Kunst, and E. J. Bergholtz, Phys. Rev. B **99**, 041406(R) (2019).
[28] R. Okugawa and T. Yokoyama, Phys. Rev. B **99**, 041202(R) (2019).
[29] H. Zhou, J. Y. Lee, S. Liu, and B. Zhen, Optica **6**, 190 (2019).
[30] T. Yoshida, R. Peters, N. Kawakami, and Y. Hatsugai, Phys. Rev. B **99**, 121101(R) (2019).
[31] F. Guinea, M. I. Katsnelson, and A. K. Geim, Nat. Phys. **6**, 30 (2010).
[32] N. Levy, S. Burke, K. Meaker, M. Panlasigui, A. Zettl, F. Guinea, A. C. Neto, and M. Crommie, Science **329**, 544 (2010).
[33] M. C. Rechtsman, J. M. Zeuner, A. Tnnermann, S. Nolte, M. Segev, and A. Szameit, Nat. Photonics **7**, 153 (2013).
[34] X. Wan, A. M. Turner, A. Vishwanath, and S. Y. Savrasov, Phys. Rev. B **83**, 205101 (2011).
[35] H. Shen, B. Zhen, and L. Fu, Phys. Rev. Lett. **120**, 146402 (2018).
[36] S. Yao and Z. Wang, Phys. Rev. Lett. **121**, 086803 (2018).
[37] S. Yao, F. Song, and Z. Wang, Phys. Rev. Lett. **121**, 136802 (2018).

[38] F. K. Kunst, E. Edvardsson, J. C. Budich, and E. J. Bergholtz, Phys. Rev. Lett. **121**, 026808 (2018).
[39] Z. Gong, Y. Ashida, K. Kawabata, K. Takasan, S. Higashikawa, and M. Ueda, Phys. Rev. X **8**, 031079 (2018).
[40] H. Zhou and J. Y. Lee, Phys. Rev. B **99**, 235112 (2019).
[41] K. Kawabata, K. Shiozaki, M. Ueda, and M. Sato, Phys. Rev. X **9**, 041015 (2019).
[42] D. S. Borgnia, A. J. Kruchkov, and R.-J. Slager, Phys. Rev. Lett. **124**, 056802 (2020).
[43] A. Mostafazadeh, J. Math. Phys. (N.Y.) **43**, 205214 (2002).
[44] See Supplemental Material at http://link.aps.org/supplemental/10.1103/PhysRevLett.124.236403 for detailed discussions of the consequences of the non-Hermitian symmetries, analytic derivation of the low-energy Hamiltonian and the non-Hermitian Landau levels, and full-wave simulations of realistic acoustic metamaterials realizing proposed models, which includes Refs. [43,45–53].
[45] M. Xiao, W.-J. Chen, W.-Y. He, and C. T. Chan, Nat. Phys. **11**, 920 (2015).
[46] F. Li, X. Huang, J. Lu, J. Ma, and Z. Liu, Nat. Phys. **14**, 30 (2018).
[47] Z. Yang, F. Gao, Y. Yang, and B. Zhang, Phys. Rev. Lett. **118**, 194301 (2017).
[48] V. Peri, M. Serra-Garcia, R. Ilan, and S. D. Huber, Nat. Phys. **15**, 357 (2019).
[49] H. Xue, Y. Yang, F. Gao, Y. Chong, and B. Zhang, Nat. Mater. **18**, 108 (2019).
[50] X. Ni, M. Weiner, A. Alù, and A. B. Khanikaev, Nat. Mater. **18**, 113 (2019).
[51] R. Fleury, D. Sounas, and A. Alu, Nat. Commun. **6**, 1 (2015).
[52] K. Ding, G. Ma, M. Xiao, Z. Q. Zhang, and C. T. Chan, Phys. Rev. X **6**, 021007 (2016).
[53] X. Wen, C. Qiu, Y. Qi, L. Ye, M. Ke, F. Zhang, and Z. Liu, Nat. Phys. **15**, 352 (2019).
[54] H. Schomerus and N. Y. Halpern, Phys. Rev. Lett. **110**, 013903 (2013).
[55] X.-X. Zhang and M. Franz, Phys. Rev. Lett. **124**, 046401 (2020).
[56] T. Baba, Nat. Photonics **2**, 465 (2008).
[57] C. Monat, B. Corcoran, M. Ebnali-Heidari, C. Grillet, B. J. Eggleton, T. P. White, L. O'Faolain, and T. F. Krauss, Opt. Express **17**, 2944 (2009).
[58] D. I. Pikulin, A. Chen, and M. Franz, Phys. Rev. X **6**, 041021 (2016).
[59] Y. D. Chong, X.-G. Wen, and M. Soljacic, Phys. Rev. B **77**, 235125 (2008).
[60] J. Noh, S. Huang, D. Leykam, Y. D. Chong, K. P. Chen, and M. C. Rechtsman, Nat. Phys. **13**, 611 (2017).
[61] W.-J. Chen, M. Xiao, and C. T. Chan, Nat. Commun. **7**, 13038 (2016).
[62] C. Fang, H. M. Weng, X. Dai, and Z. Fang, Chin. Phys. B **25**, 117106 (2016).
[63] A. Szameit and S. Nolte, J. Phys. B **43**, 163001 (2010).
[64] J. M. Zeuner, M. C. Rechtsman, Y. Plotnik, Y. Lumer, S. Nolte, M. S. Rudner, M. Segev, and A. Szameit, Phys. Rev. Lett. **115**, 040402 (2015).
[65] M. C. Rechtsman, J. M. Zeuner, Y. Plotnik, Y. Lumer, D. Podolsky, F. Dreisow, S. Nolte, M. Segev, and A. Szameit, Nature (London) **496**, 196 (2013).
[66] C. H. Lee, S. Imhof, C. Berger, F. Bayer, J. Brehm, L. W. Molenkamp, T. Kiessling, and R. Thomale, Commun. Phys. **1**, 39 (2018).
[67] T. Hofmann, T. Helbig, C. H. Lee, M. Greiter, and R. Thomale, Phys. Rev. Lett. **122**, 247702 (2019).
[68] S. Liu, S. Ma, C. Yang, L. Zhang, W. Gao, Y. J. Xiang, T. J. Cui, and S. Zhang, Phys. Rev. Applied **13**, 014047 (2020).
[69] M. Hafezi, E. A. Demler, M. D. Lukin, and J. M. Taylor, Nat. Phys. **7**, 907 (2011).
[70] D. Leykam, S. Mittal, M. Hafezi, and Y. D. Chong, Phys. Rev. Lett. **121**, 023901 (2018).
[71] S. Mittal, V. V. Orre, D. Leykam, Y. D. Chong, and M. Hafezi, Phys. Rev. Lett. **123**, 043201 (2019).
[72] H. Zhao, X. Qiao, T. Wu, B. Midya, S. Longhi, and L. Feng, Science **365**, 1163 (2019).